The intermediate polar cataclysmic variable GK Persei 120 years after the nova explosion: a first dynamical mass study

A. Álvarez-Hernández[1,2]⋆, M. A. P. Torres[1,2], P. Rodríguez-Gil[1,2], T. Shahbaz[1,2],
G. C. Anupama[3], K. D. Gazeas[4], M. Pavana[3,5], A. Raj[6], P. Hakala[7], G. Stone[8],
S. Gomez[9], P. G. Jonker[10,11], J.-J. Ren[12], G. Cannizzaro[10,11], I. Pastor-Marazuela[13,14],
W. Goff[15], J. M. Corral-Santana[16], R. Sabo[17]

[1]*Instituto de Astrofísica de Canarias, E-38205 La Laguna, Tenerife, Spain*
[2]*Departamento de Astrofísica, Universidad de La Laguna, E-38206 La Laguna, Tenerife, Spain*
[3]*Indian Institute of Astrophysics, 560 034 Bangalore, India*
[4]*Section of Astrophysics, Astronomy and Mechanics, Department of Physics, National and Kapodistrian University of Athens, GR-15784 Zografos, Athens, Greece*
[5]*Department of Physics, Pondicherry University, Puducherry 605014, India*
[6]*Dept. of Physics & Astrophysics, University Road, University Enclave, Delhi 110007, India*
[7]*Finnish Centre for Astronomy with ESO (FINCA), Quantum, University of Turku, FI-20014, Turku, Finland*
[8]*First Light Observatory Systems, 9 Wildflower Way, Santa Fe, NM 87506 USA*
[9]*Center for Astrophysics | Harvard & Smithsonian, 60 Garden Street, Cambridge, MA 02138, USA*
[10]*SRON, Netherlands Institute for Space Research, Sorbonnelaan 2, 3584 CA, Utrecht, The Netherlands*
[11]*Department of Astrophysics/ IMAPP, Radboud University, Heyendaalseweg 135,6525 AJ, Nijmegen, The Netherlands*
[12]*CAS Key Laboratory of Space Astronomy and Technology, National Astronomical Observatories, Chinese Academy of Sciences, Beijing 100101, People's Republic of China*
[13]*Anton Pannekoek Institute, University of Amsterdam, Postbus 94249, 1090 GE Amsterdam, The Netherlands*
[14]*ASTRON, the Netherlands Institute for Radio Astronomy, Oude Hoogeveensedijk 4, 7991 PDDwingeloo, The Netherlands*
[15]*American Association of Variable Star Observers, 49 Bay State Rd. Cambridge, MA 02138*
[16]*European Southern Observatory, Alonso de Córdova 3107, Vitacura, Casilla 19001, Santiago de Chile, Chile*
[17]*American Association of Variable Star Observers, 1344 Post Dr. Bozeman, MT 59715*

ABSTRACT
We present a dynamical study of the intermediate polar and dwarf nova cataclysmic variable GK Per (Nova Persei 1901) based on a multi-site optical spectroscopy and R-band photometry campaign. The radial velocity curve of the evolved donor star has a semi-amplitude $K_2 = 126.4 \pm 0.9 \, \mathrm{km \, s^{-1}}$ and an orbital period $P = 1.996872 \pm 0.000009 \, \mathrm{d}$. We refine the projected rotational velocity of the donor star to $v_{\rm rot} \sin i = 52 \pm 2 \, \mathrm{km \, s^{-1}}$ which, together with K_2, provides a donor star to white dwarf mass ratio $q = M_2/M_1 = 0.38 \pm 0.03$. We also determine the orbital inclination of the system by modelling the phase-folded ellipsoidal light curve and obtain $i = 67° \pm 5°$. The resulting dynamical masses are $M_1 = 1.03^{+0.16}_{-0.11} \, \mathrm{M_\odot}$ and $M_2 = 0.39^{+0.07}_{-0.06} \, \mathrm{M_\odot}$ at 68 per cent confidence level. The white dwarf dynamical mass is compared with estimates obtained by modelling the decline light curve of the 1901 nova event and X-ray spectroscopy. The best matching mass estimates come from the nova light curve models and an X-ray data analysis that uses the ratio between the Alfvén radius in quiescence and during dwarf nova outburst.

Key words: accretion, accretion discs – binaries: close – novae, cataclysmic variables – stars: individual: GK Per (Nova Persei 1901)

1 INTRODUCTION

Cataclysmic variables (CVs) are binary systems where a non-degenerate star fills its Roche lobe and transfers matter towards an accreting white dwarf (WD; Kraft 1964, see Warner 1995 and references therein). For a weakly magnetic WD, the mass from the donor star is accreted onto the surface via an accretion disc. In magnetic CVs, however, the magnetic field is strong enough to dominate at least

part of the accretion flow. Polars are the most extreme magnetic CVs: the strong WD magnetic field ($B \gtrsim 10^7 \, \mathrm{G}$) prevents the formation of an accretion disc and forces the transferred material to follow the field lines onto one or both poles of the WD (Chanmugam & Wagner 1977; see Cropper 1990 for a review). In contrast, in intermediate polars (IPs) the magnetic field is only able to take control over the transferred plasma in close proximity to the WD (Patterson 1994). In these systems, the accretion disc is truncated at a certain radius from the WD and the disc accretion flow is funneled from there to its magnetic poles along the field lines. A remarkable difference between

⋆ E-mail: ayozeav@iac.es

both types of magnetic CV is the degree of synchronization of the WD spin with the orbit: in IPs the spin period is usually significantly shorter than the orbital period, while both periods are nearly equal for most polars (see e.g. Norton et al. 2004).

GK Per was discovered as a nova on 1901 February 22 by Scottish amateur astronomer Thomas David Anderson (Williams 1901). It peaked at a visual apparent magnitude of 0.2 mag. After years of irregular fluctuations in brightness with amplitudes up to 1.5 mag and several dozens of days duration, in 1948 it reached a quiescence state ($m_V \simeq 13$ mag) and started to show $1-3$-mag dwarf nova outbursts that typically last 50 d and recur about every three years (Hudec 1981; Bianchini et al. 1982; Sabbadin & Bianchini 1983; Šimon 2002).

Crampton et al. (1986) reported a binary orbital period of nearly 2 d and Watson et al. (1985) found a WD spin period of 351 s in the modulation of the hard X-ray emission, thus confirming the IP nature of GK Per. The spin period also modulates the U-band flux (Patterson 1991) and the equivalent width of the emission lines at optical wavelengths (Garlick et al. 1994; Reinsch 1994). J-band circular polarimetry of GK Per in quiescence is consistent with a null detection (Stockman et al. 1992). However, the intensity of the WD magnetic field is estimated at $B \sim 10^5$ G from X-ray spectral modelling (Wada et al. 2018).

The geometrical, kinematic and physical properties of the nova shell in GK Per as well as its interaction with its surroundings have been studied in detail at different frequencies (Seaquist et al. 1989; Scott et al. 1994; Anupama & Kantharia 2005; Liimets et al. 2012, and references therein). In particular, far-infrared observations showed that the nova shell is embedded in an ancient, possibly bipolar planetary nebula centred on the binary and extending ≈ 17 arcmin to the NW and SE (Dougherty et al. 1996). At the time of its discovery, this nebula was interpreted as being the remnant of the binary common envelope phase (Bode et al. 1987). However, ejecta presumably from the WD progenitor star expelled during a second asymptotic giant branch phase (and thus a second common envelope event), triggered by a period of high mass transfer rate from the donor star ($> 3 \times 10^{-7}$ M$_\odot$ yr^{-1} = 1.9×10^{19} g s^{-1}), was proposed as a more likely origin for the nebula (Dougherty et al. 1996).

Several spectroscopic classifications of the donor star in GK Per have been reported by different authors: K2 V–IVp (Kraft 1964; Gallagher & Oinas 1974), K0 III–IV (Crampton et al. 1986), K2–3 V (Reinsch 1994) and K1 IV (Morales-Rueda et al. 2002, hereinafter MR02). MR02 presented a radial velocity study of the donor star building on similar work by Kraft (1964), Crampton et al. (1986) and Reinsch (1994) that provided an orbital period $P = 1.9968 \pm 0.0008$ d, a radial velocity semi-amplitude $K_2 = 120.5 \pm 0.7$ km s^{-1} and a systemic velocity $\gamma = 40.8 \pm 0.7$ km s^{-1}. MR02 also reported an estimate of the projected rotational velocity of the donor star on the line of sight of the observer ($v_{rot} \sin i = 61.5 \pm 11.8$ km s^{-1}) and a donor-to-WD mass ratio $q = 0.55 \pm 0.21$. In obtaining these values they used optical spectra with ≈ 120 km s^{-1} full-width at half-maximum (FWHM) resolution. Harrison & Hamilton (2015) obtained $v_{rot} \sin i = 55 \pm 10$ km s^{-1} from near-infrared spectra with ≈ 12 km s^{-1} FWHM spectral resolution.

Precise dynamical masses of the two stars in GK Per have never been determined because the orbital inclination has remained largely unconstrained. The absence of eclipses in the light curves at optical wavelengths suggested an inclination $i < 73°$ (Reinsch 1994), which translates to lower limits on the masses of the WD and the donor star of $M_1 > 0.87 \pm 0.24$ M$_\odot$ and $M_2 > 0.48 \pm 0.32$ M$_\odot$, respectively (MR02). WD masses of $M_1 = 1.15 \pm 0.05$ M$_\odot$ and $M_1 = 1.22 \pm 0.10$ M$_\odot$ have been derived from modelling of the nova light curve

by Hachisu & Kato (2007) and Shara et al. (2018), respectively. In addition, estimates of the WD mass ranging from $0.52^{+0.34}_{-0.16}$ to 1.24 ± 0.10 M$_\odot$ have been obtained through modelling of X-ray spectra (see Section 4 for details).

In this work, we present the first dynamical study of GK Per that yields reliable masses for the WD and the donor star. The paper is structured as follows: in Section 2 we describe the time-resolved optical photometry and spectroscopy observations and the data reduction. From the analysis of the absorption lines of the donor star we obtain its radial velocity curve (Section 3.1), constrain its spectral type (Section 3.2) and determine its rotational broadening (Section 3.3). In Section 3.4 we present the modelling of the R-band light curve, which provides the orbital inclination for the first time. The stellar dynamical masses are then obtained using the measured quantities. These are discussed in Section 4, where we also compare the WD dynamical mass with the available estimates from X-ray spectral fitting and modelling of the nova light curve. Finally, we draw our conclusions in Section 5.

2 OBSERVATIONS AND DATA REDUCTION

The 1.9968-d orbital period of GK Per makes a given orbital phase occur 4.6 min earlier every next orbital cycle. In addition, during a typical 10-h observing night only 20 per cent of the orbit can be covered. Thus, the fact that the orbital period is close to an integer number of days precludes ground-based observers at a single location from achieving entire photometric coverage of the orbit in contemporaneous nights. This makes the light curve strongly susceptible to aperiodic night-to-night accretion variability. To overcome this difficulty and thus obtain the full ellipsoidal modulation produced by the donor star, we performed multi-site photometry between 2017 December and 2018 January. We also took multi-site spectroscopy during 2017–2019 to improve the light curve modelling and obtain a full dynamical determination of the system parameters.

In this Section, we describe all the collected data sets. Tables 1 and 2 summarize the spectroscopic and photometric observations, respectively. Note that we have adopted orbital phase 0 as the moment of inferior conjunction of the donor star.

2.1 Spectroscopy

The optical spectroscopy data of GK Per were obtained in 2017–2019 using four telescopes. We planned the observations in order to cover the orbital phases that better define the radial velocity curve (0.25 and 0.75) and $v_{rot} \sin i$. The spectral resolution of all our data sets was slit limited. Only the seeing of the 2019 September 7 WHT data ($0.7-0.8$ arcsec) was slightly less than the slit width (0.8 arcsec), but this was checked to have a negligible influence on the results. Except where indicated, in each observing run we observed the spectral templates HD 20165 and HR 2556, which are classified as K1 V (Koen et al. 2010) and K0 III–IV (Luck 2015) stars and have low intrinsic radial velocities of -16.92 ± 0.19 km s^{-1} and 27.68 ± 0.17 km s^{-1}, respectively (Gaia Collaboration et al. 2018). Their rotational broadenings are also small: 1.6 km s^{-1} for HD 20165 (Brewer et al. 2016) and 4.3 km s^{-1} for HR 2556 (Luck 2015).

2.1.1 Himalayan Chandra Telescope

The first data set was taken with the 2-m Himalayan Chandra Telescope (HCT) located in the Indian Astronomical Observatory,

Saraswati Mount, India. The Hanle Faint Object Spectrograph Camera (HFOSC) was used with grism #8 and a 0.77-arcsec slit width. This instrumental configuration provided spectra in the wavelength range $5120 - 9310$ Å with a dispersion of 1.27 Å pix^{-1} and a FWHM spectral resolution of 5.6 Å (equivalent to $\simeq 270$ km s^{-1} at 6300 Å). We took 20, 24 and 21 spectra using exposure times between 900 and 1200 s on the nights of 2017 December 6, 7 and 8, respectively. FeNe calibration arc lamps were taken often. According to the ephemeris (Section 3.1), these observations covered time intervals near the quadratures of the orbit. The seeing measured from the spectral traces was $1.7 - 3.6$ arcsec during the first night, $1.7 - 3.2$ arcsec on the second night and $1.7 - 2.6$ arcsec on the last night.

2.1.2 Nordic Optical Telescope

We took a second data set with the 2.56-m Nordic Optical Telescope (NOT) sited in the Observatorio del Roque de los Muchachos on La Palma, Spain. We used the Alhambra Faint Object Spectrograph and Camera (ALFOSC) with grism #8 and a 0.5-arcsec slit width. This setup yields a wavelength coverage $5680 - 8580$ Å, a dispersion of 1.41 Å pix^{-1} and a FWHM spectral resolution of 3.5 Å (equivalent to $\simeq 170$ km s^{-1} at 6300 Å). These observations were conducted on the nights of 2017 December 8, 9 and 10, when we obtained 30, 21 and 16 spectra, respectively. The exposure time varied between 600 and 900 s. Spectra of HeNe + ThAr calibration arc lamps were taken after each target exposure. This data set covered orbital phase ranges around 0 and 0.5. The seeing was $1.1 - 2.1$, $1.0 - 1.2$ and $0.9 - 1.5$ arcsec on the first, second and third night, respectively.

2.1.3 William Herschel Telescope

In order to obtain further radial velocities and to measure the rotational broadening of the absorption lines of the donor star, we used the Intermediate-dispersion Spectrograph and Imaging System (ISIS) attached to the 4.2-m William Herschel Telescope (WHT), also located in the Observatorio del Roque de los Muchachos. We took a total of 24 optical spectra during seven nights between 2018 December 1 and 2019 September 13 using the R600R and the R1200R gratings with different slit widths and central wavelengths (see Table 1). The FWHM spectral resolutions at 6300 Å were ≤ 61 and ≤ 36 km s^{-1} for the R600R and the R1200R gratings, respectively. CuNe + CuAr arc lamp spectra were taken just after each target spectrum for wavelength calibration. The spectral templates were only observed with the R1200R grating. In chronological order, the seeing of the WHT spectra was $1.0 - 1.2$, $0.9 - 1.1$, ~ 0.8, $0.7 - 0.8$, $3.8 - 3.9$, $1.1 - 1.3$ and $1.3 - 1.4$ arcsec.

2.1.4 Xinglong 2.16-m Telescope

Four spectra close to orbital phase 0.75 were taken with the 2.16-m telescope at the Xinglong Observatory, China, on 2019 November 14. We used the Beijing-Faint Object Spectrograph and Camera (BFOSC) with the G8 grating and a 1.1-arcsec slit width. The spectral range covered was $6000 - 7550$ Å with a dispersion of 1.09 Å pix^{-1} and a FWHM spectral resolution of 4.8 Å (equivalent to $\simeq 228$ km s^{-1} at 6300 Å). We took a spectrum of a FeAr + Ne arc lamp after each target exposure for wavelength calibration. The seeing varied between 3.0 and 4.0 arcsec.

Table 1. Log of the spectroscopy observations with the Himalayan Chandra Telescope (HCT), Nordic Optical Telescope (NOT), William Herschel Telescope (WHT) and the 2.16-m telescope at the Xinglong Observatory. The gratings and slit widths (in arcsec) used at the WHT are given in brackets.

Telescope/instrument Date	#	$T_{\rm exp}$ (s)	Coverage (Å)	$\Delta\lambda$ (Å)
HCT/HFOSC				
2017 Dec 6	20	600–900	5120–9310	5.6
2017 Dec 7	24	900–1200	"	"
2017 Dec 8	21	1200	"	"
NOT/ALFOSC				
2017 Dec 8	30	600–900	5680–8580	3.5
2017 Dec 9	21	600	"	"
2017 Dec 10	16	600	"	"
WHT/ISIS				
2018 Dec 1 (R1200R, 1.0)	6	300	5830–6600	0.75
2019 Aug 24 (R600R, 0.7)	4	300	5460-6940	1.27
2019 Aug 25 (R600R, 0.7)	2	300	5460-6940	1.27
2019 Sep 7 (R1200R, 0.8)	4	300	5830–6575	0.60
2019 Sep 8 (R1200R, 1.0)	4	300	5830–6575	0.75
2019 Sep 12 (R1200R, 0.8)	4	300	5830–6575	0.60
2019 Sep 13 (R1200R, 0.8)	4	300	5830–6575	0.60
2.16-m Xinglong/BFOSC				
2019 Nov 14	4	900	6000–7550	4.8

2.2 Photometry

Time-resolved R-band photometry was obtained with four telescopes at different geographical longitudes to achieve a good sampling of almost the entire binary orbit. These photometric data were obtained in the period 2017 December–2018 February. Some of the nights were either close in time (< 1 d) or simultaneous with the NOT and HCT spectroscopy. We used the simultaneous photometry and spectroscopy observations to correct for night-to-night variability in the light curve caused by accretion (Section 3.4.1). The observing log is presented in Table 2.

2.2.1 J. C. Bhattacharya Telescope

We obtained time-resolved R-band photometry of GK Per during four nights (2017 December 7–10) using the 1.3-m J. C. Bhattacharya Telescope (JCBT) in the Vainu Bappu Observatory on the Javadi hills of Tamilnadu, India. This photometry is in part simultaneous with some NOT and HCT spectroscopic data sets (Sections 2.1.1 and 2.1.2).

We imaged the GK Per field with the Peltier-cooled Princeton Instruments ProEM CCD camera, an array of 1024×1024 13-μm square pixels. This delivers a usable field of view (FOV) of 4.3×4.3 arcmin and a pixel size on the sky of 0.26 arcsec. The full-frame, high-gain (5 MHz frequency) readout mode yielded 1.19 e^{-} ADU^{-1} and a readout noise of 13 e^{-}. We used the Bessel R filter and fixed the exposure time at 600 s.

2.2.2 0.4-m University of Athens Observatory

We used the University of Athens Observatory (UOAO), Greece, 0.4-m robotic and remotely controlled telescope (Gazeas 2016) to obtain time-resolved R-band photometry of the target on five nights

in 2017 December and a further five in 2018 January. Part of the photometry (2017 December 8–10) is simultaneous with some HCT and NOT spectroscopic data sets (Sections 2.1.1 and 2.1.2).

We observed GK Per with the SBIG ST10 CCD camera, an array of 2184×1472 6.8-μm square pixels, binned at 2×2. The FOV was increased to 17×26 arcmin with the use of an f/6.3 focal reducer, resulting in a plate scale of 1.39 arcsec pixel^{-1}. The CCD gain is $1.32\,\mathrm{e^-\,ADU^{-1}}$ and the readout noise $8.8\,\mathrm{e^-}$. We used the Johnson-Cousins R filter and an exposure time of 60 s.

2.2.3 0.3-m Sutter Creek Observatory

The 0.3-m SC30 telescope located at the Sutter Creek Observatory in California, USA, also provided time-resolved R-band photometry of GK Per on the nights of 2018 January 21 and 28. The observations were carried out with the unbinned 1024×1024 CCD array of 24-μm pixels. The images cover a 28×28 arcmin FOV with a plate scale of 1.65 arcsec pixel^{-1}. The CCD readout has a gain of $0.69\,\mathrm{e^-\,ADU^{-1}}$ and a readout noise of $2.81\,\mathrm{e^-}$. We used the Johnson-Cousins R filter and the exposure time was fixed at 60 s.

2.2.4 0.43-m Sierra Remote Observatories

The 0.43-m f/6.8 CDK telescope at the Sierra Remote Observatories in California, USA, provided further time-resolved R-band photometry of GK Per on 2018 January 25–30 and February 1–3. The target field was imaged on the 2×2 binned 2004×1336 CCD array of 18-μm square pixels of the SBIG STXL-11002 camera. This provided a FOV of 42×29 arcmin and a plate scale of 1.26 arcsec pixel^{-1}. The readout gain was $1.74\,\mathrm{e^-\,ADU^{-1}}$ and the readout noise $15\,\mathrm{e^-}$. We used the Johnson-Cousins R filter with an exposure time of 60 s.

2.2.5 TESS photometry

The Transiting Exoplanet Survey Satellite (*TESS*) is a space-based optical telescope launched in 2018 to perform an all-sky survey to search for transiting exoplanets (Ricker et al. 2015). The telescope consists of four cameras, each with a FOV of $24° \times 24°$. This results in a combined telescope FOV of $24° \times 96°$. The size of each camera is 4096×4096 pixel and the plate scale is 21 arcsec pixel^{-1}. Ninety per cent of the flux of a star is contained within a 4×4 pixel (1.4×1.4 arcmin) region around its centroid (Ricker et al. 2015). *TESS* observations are performed in a single photometric band that covers a broad wavelength range from about 6000 to 11000 Å.

The satellite observed GK Per (*TESS* Input Catalog, TIC 431762266) on 2019 November 3–12 and 15–27 (sector 18). The full-frame images of this sector were taken with a cadence of 30 min by combining 900 2-s exposures.

2.3 Data reduction

All the spectra were reduced, wavelength calibrated and extracted following standard techniques implemented in IRAF[1] and PAMELA (Marsh 1989, available in the STARLINK distribution[2]). For the NOT and HCT data the pixel-to-wavelength scale was determined with six-term polynomial fits to 33 and 35 arc lines, respectively. For the WHT and Xinglong telescopes we performed third-order spline fits

---

[1] IRAF is distributed by the National Optical Astronomy Observatories.

[2] https://starlink.eao.hawaii.edu/starlink

Table 2. Log of the time-resolved R-band photometry.

Telescope Date	#	$T_{\exp}$ (s)	Coverage (h)
1.3-m JCBT			
2017 Dec 7	37	600	8.2
2017 Dec 8	41	600	6.9
2017 Dec 9	50	600	8.1
2017 Dec 10	46	600	8.0
0.4-m UOAO telescope			
2017 Dec 8	135	60	9.9
2017 Dec 9	310	60	9.1
2017 Dec 10	594	60	10.7
2017 Dec 11	517	60	9.3
2017 Dec 01	593	60	11.1
2018 Jan 27	400	60	7.2
2018 Jan 28	220	60	3.9
2018 Jan 29	385	60	6.9
2018 Jan 30	343	60	6.2
2018 Jan 31	316	60	6.4
0.3-m SC30 telescope			
2018 Jan 21	178	60	3.6
2018 Jan 28	197	60	4.1
0.43-m CDK telescope			
2018 Jan 25	195	60	5.5
2018 Jan 26	230	60	5.2
2018 Jan 27	171	60	5.5
2018 Jan 28	250	60	5.5
2018 Jan 30	173	60	3.8
2018 Feb 01	150	60	3.4
2018 Feb 02	250	60	5.5
2018 Feb 03	100	60	3.3

to 16/23 (R600R/R1200R gratings) and 17 arc lines, respectively. The rms scatter of the fits was < 0.05 Å for all data sets. We used the [O I] 6300.304 Å sky emission line to look for wavelength zero-point deviations and found they were smaller than the rms scatter of the fitted wavelength calibration, except for the HCT data for which they reach $\simeq 10$ km s^{-1}. Hence, we only corrected for these offsets in that case.

The extracted spectra were imported into MOLLY[3] in order to do the analysis described in the next sections and corrected for the Earth motion to have them in the heliocentric rest frame. Times are expressed in heliocentric Julian days (UTC). Finally, they were normalised using a seventh-order polynomial fit to the continuum after masking the strong emission lines.

The R-band images were debiased and flat-fielded using the standard CCD data processing workflow within IRAF. Differential photometry with variable aperture was performed with the HiPERCAM pipeline[4]. For this purpose, we used the field stars GK Per–12 ($r \simeq 13.4$ mag) and GK Per–10 ($r \simeq 14.4$ mag) labelled in Henden & Honeycutt (1995, 1997) as the comparison and check star, respectively.

We obtained the *TESS* light curve from the 30-min full-frame

---

[3] http://deneb.astro.warwick.ac.uk/phsaap/software/molly/html/INDEX.html

[4] https://github.com/HiPERCAM

images using the TESSERACT[5] package (Rojas et al., in prep.) that performs aperture photometry via TESSCut (Brasseur et al. 2019) and LIGHTKURVE (Lightkurve Collaboration et al. 2018). Visual inspection of the GK Per field revealed some contaminating stars given the limited angular resolution of the *TESS* images. Using the *Aladin Sky Atlas*[6] and the Pan–STARRS Data Release 1 (Chambers et al. 2016) we checked that the six brightest objects in the 4×4 pixel region around GK Per have $r = 14.7 - 17.8$ mag, fainter than GK Per ($r \simeq 12.7$ mag) and non-variable. Hence, these contaminating stars only add a constant veiling to the GK Per light curve. We used an on-target photometric aperture of one pixel in order to minimise this contamination. A larger circular aperture was checked to result in a significant decrease of the light curve amplitude.

3 ANALYSIS AND RESULTS

All uncertainties presented in this and the next sections are quoted at 68 per cent confidence unless otherwise stated.

3.1 Radial velocity curve of the donor star

We measured the radial velocities of the donor absorption lines by cross-correlating each GK Per spectrum with the spectrum of the K1 V HD 20165 template star in the spectral range $6050 - 6538$ Å, after masking the diffuse interstellar band at ≈ 6280 Å. Prior to this, the template spectrum was corrected for its systemic velocity and for any wavelength zero-point offset by removing the velocity measured by Gaussian fitting the core of the Hα absorption line. Also, all the spectra were re-binned on to a common constant velocity scale. We proceeded in the same way with the K0 III-IV HR 2556 template, which resulted in very similar values of the radial velocities. To account for all uncertainties, the rms of the wavelength calibration was added linearly to the statistical uncertainty of each radial velocity measurement. Since there is no evidence for irradiation of the donor star (see Section 3.3), we performed least-squares sinusoidal fits to the radial velocities, $V(t)$, of the form:

$$V(t) = \gamma + K_2 \sin \left[\frac{2\pi}{P} (t - T_0) \right], \tag{1}$$

where γ is the heliocentric systemic velocity, K_2 the radial velocity semi-amplitude of the donor star, P the orbital period and T_0 the time of closest approach of the donor star to the observer. Fig. 1 shows the radial velocity curve and the best fit. In our preliminary fits, the HCT/HFOSC radial velocities showed a large scatter that the rest of data did not at similar orbital phases, with a deviation of up to 45-σ from the initial best fit. We could not identify the reason for this and we excluded these data from the fitting process. In addition, one NOT/ALFOSC radial velocity point was discarded since its deviation was larger than 7-σ. After rejecting these deviant points, the χ^2 relative to the number of degrees of freedom (dof), χ^2/dof, was $\simeq 1.6$ for both templates. We followed by rescaling the radial velocity uncertainties by a factor $\simeq 1.26$ so that the χ^2/dof of the fit was 1.0. The best-fit parameters for each template are listed in Table 3.

We obtained an orbital period that agrees within 1-σ of the value $P = 1.9968 \pm 0.0008$ d reported in MR02. Our K_2 determination agrees within 1-σ of the value $K_2 = 124 \pm 2$ km s^{-1} reported by

Crampton et al. (1986). Their coverage of the radial velocity curve only showed small gaps around orbital phases 0.0, 0.35, 0.45 and 0.9, and they achieved a good sampling of the orbit quadratures[7]. On the other hand, our K_2 is only consistent with $K_2 = 120.5 \pm 0.7$ km s^{-1} obtained by MR02 at the 4-σ level. They cover the orbital phases 0.0 to 0.3 and 0.5 to 0.8. However, their radial velocity curve displays a significant number of departing points at phases $0.25 - 0.30$, which probably acted to lower the amplitude of their best sine fit (see fig. 3 in their paper). These authors also obtained a value of $K_2 = 129 \pm 2.7$ km s^{-1} (consistent with ours at the 1-σ level) by combining the radial velocities measured by Kraft (1964), Crampton et al. (1986) and Reinsch (1994). Finally, Crampton et al. (1986) and MR02 obtained a systemic velocity of 28 ± 1 and 40.8 ± 0.7 km s^{-1}, respectively. Our best-fit $\gamma \simeq 32$ km s^{-1} lies between those two values, but is much closer to the Crampton et al.'s estimate.

3.2 Spectral classification of the donor star

The orbital period-mean density (ρ_2) relation for Roche lobe-filling stars (Faulkner et al. 1972) yields ρ_2 (g/cm^3) $\simeq 110 P(\mathrm{h})^{-2} = 0.048$ g/cm$^3 = 0.034 \rho_\odot$ for the evolved donor star in GK Per. This value is in between those expected for main sequence and giant stars (e.g. $\simeq 1.26 \rho_\odot$ and $\simeq 0.00031 \rho_\odot$ for K0 V and K0 III, respectively, Cox 2000). In order to constrain the spectral type of the donor star we used two grids of high resolution ($R = \lambda/\Delta\lambda \simeq 60000$) templates covering $4990 - 6410$ Å and extracted from the library published in Yee et al. (2017). The first grid (Table 4) contains nine spectra of main sequence stars ($\log g = 4.4 - 4.6$ dex) in the range G3 V–K4 V with -0.10 dex $<$ [Fe/H] < 0.10 dex metallicity. The spectral type of each template was determined according to its effective temperature (Yee et al. 2017) and the canonical value for each spectral type (Pecaut & Mamajek 2013). The second grid (Table 5) includes eight spectra of subgiant stars with $\log g = 3.0 - 3.6$ dex, which is close to the surface gravity of the donor star in GK Per (Section 4.1). This grid covers effective temperatures from $\simeq 4800$ to $\simeq 5300$ K and its metallicity is also -0.10 dex $<$ [Fe/H] < 0.10 dex.

We used the WHT/ISIS R1200R spectra taken on 2019 September 12 and 13 that cover the orbital phases 0.5 and 0.96, respectively. We selected these data sets to search for potential phase-dependent changes in the spectral classification due to irradiation of the inner face of the donor star by the WD and/or accretion structures. The templates were downgraded to match the resolution of the GK Per spectra by convolution with Gaussian profiles. Then, we applied the optimal subtraction technique described in Marsh et al. (1994) to every template. We performed this analysis in the spectral range $6050 - 6400$ Å. We proceeded as follows: we corrected for the radial velocity of each GK Per spectrum to velocity-shift them to the rest frame of the template. Next, we computed a weighted average of the GK Per spectra giving larger weights to those with higher signal-to-noise ratio. We subsequently broadened the photospheric lines of the template spectra by convolution with the Gray's rotational profile (Gray 1992), probing the $v_{\mathrm{rot}} \sin i$ space between 1 and 150 km s^{-1} in steps of 1 km s^{-1}. A robust measurement of $v_{\mathrm{rot}} \sin i$ will be given in Section 3.3, where we will use templates taken with the same instrumental setup as the GK Per data. We used a linear limb-darkening coefficient of 0.65, a reasonable choice for a K0–3 IV star (Claret et al. 1995). Note that similar results are

---

[7] Note that Crampton et al. (1986) defined T_0 as the time of maximum radial velocity of the donor star and here and in Section 3.2 we provide their orbital phase coverage according to our T_0 convention.
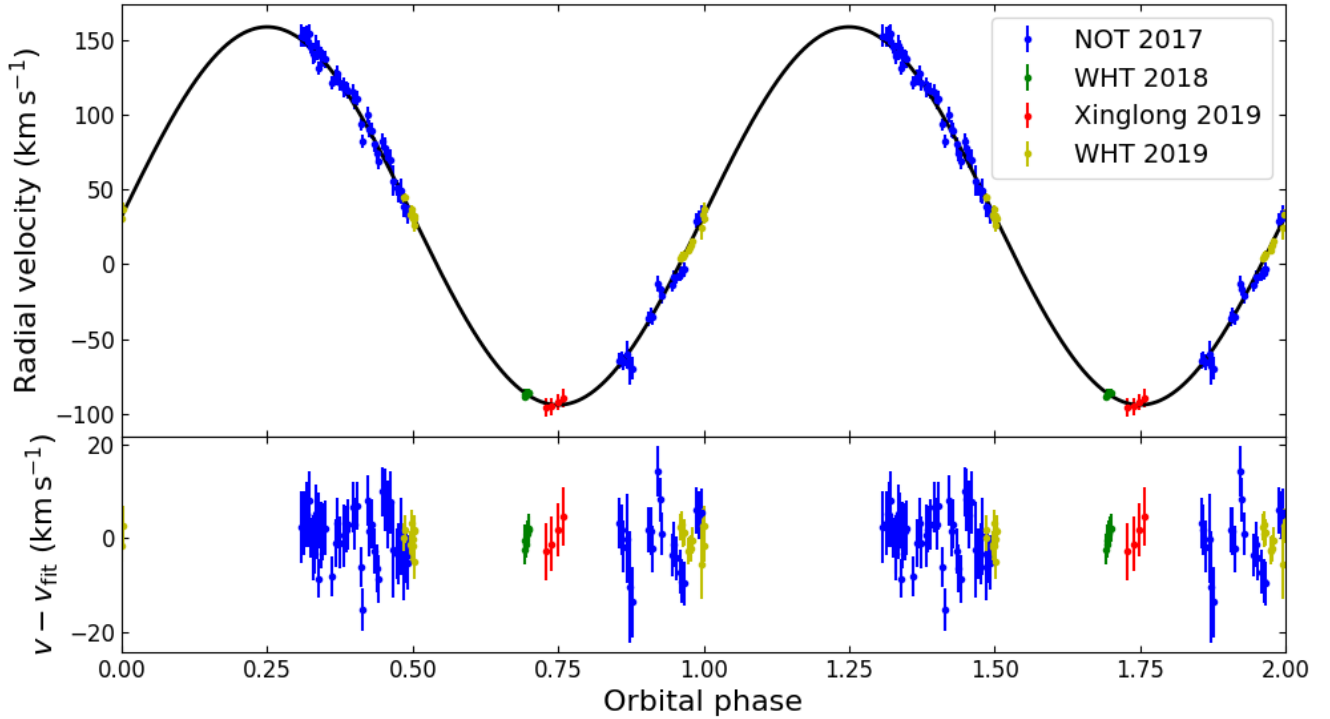
Figure 1. Top panel: Heliocentric radial velocity curve of the donor star absorption features obtained by cross-correlating the individual spectra with the spectral template HD 20165 (K1 V). The error bars have been scaled by a factor $\simeq 1.26$ to obtain a fit with $\chi^2/dof = 1.0$. The best sine fit is shown as a black line. The orbital cycle has been repeated for the sake of clarity. Bottom panel: residuals of the fit.

Table 3. Radial velocity curve best-fit parameters. The rms of the wavelength calibration was lineally added to the uncertainties of the γ values. Degrees of freedom (dof) = 94.

Template	Spectral type	γ (km s^{-1})	K_2 (km s^{-1})	P (d)	T_0 (HJD)
HD 20165	K1 V	32 ± 2	126.4 ± 0.9	1.996872 ± 0.000009	2458095.709 ± 0.002
HR 2556	K0 III-IV	33 ± 2	126.9 ± 0.9	1.996874 ± 0.000009	2458095.709 ± 0.003

obtained for values of 0.5 or 0.8. The broadened versions of each template spectrum were multiplied by a factor f between 0 and 1 and then subtracted from the weighted-average spectrum of GK Per. This factor represents the fractional contribution of the donor star to the total flux in the wavelength range of the analysis. Finally, we searched for the values of $v_{rot} \sin i$ and f that minimised the χ^2 between the residual of the subtraction and a smoothed version of itself obtained by convolution with a 15-Å FWHM Gaussian. In doing so, we compared the results of using different FWHMs (between 15 and 40 Å) for the smoothing Gaussian. The results were found to be the same within the uncertainties. The minimum χ^2/dof for each template is presented in Tables 4 and 5.

The results obtained with the main sequence templates suggest a spectral type of the donor star in the range G7–K1 with the lowest χ^2/dof value found for K1. On the other hand, the χ^2/dof values obtained with the grid of subgiant templates provide an effective temperature in the range $\simeq 4900 - 5150$ K. In this regard, Harrison (2016, see also Harrison & Hamilton 2015) characterised the chemical composition of the donor star in GK Per using near-infrared spectroscopy and synthetic spectral templates with surface gravity

log g = 4.0 dex. The effective temperature of their best-fit template was 5000 K, with an estimated uncertainty of ±110 K, in agreement with our constraint.

Kraft (1964) and Gallagher & Oinas (1974) noticed potential spectral type changes with orbital phase. However, Crampton et al. (1986) found that the average spectra at phases 0.55 and 0.05 (when we observe the hemisphere of the donor facing and trailing the WD, respectively) were consistent with being identical. Similarly, MR02 found no differences in the spectral type of the donor star between the phase intervals $0.03 - 0.28$ and $0.54 - 0.82$ when applying the optimal subtraction method to their *B*-band spectra. Our analysis also showed no noticeable changes between phases 0.5 and 0.96. We thus conclude that UV and X-ray heating of the donor star is most likely negligible during the quiescence state.

Table 4. Spectral classification of the donor star in GK Per using WHT/ISIS data and spectra of main sequence stars as templates. The number of dof is 1170.

Template	Spectral type	Effective temperature (K)	$\chi^2_{\min}$/dof at orbital phase: 0.5	0.96
HD 42807	G3 V	5730 ± 60	1.53	1.66
HD 43162	G6 V	5617 ± 60	1.54	1.64
HD 10780	G9 V	5398 ± 75	1.41	1.48
HD 72760	K0 V	5293 ± 60	1.42	1.45
HD 110743	K1 V	5198 ± 60	1.36	1.38
HD 8553	K2 V	5053 ± 60	1.53	1.52
HD 153525	K3 V	4826 ± 60	1.68	1.66
HIP 118261	K4 V	4615 ± 214	1.89	1.87

Table 5. Spectral classification of the donor star in GK Per using WHT/ISIS data and spectra of subgiant stars as templates. The number of dof is 1170.

Template	Effective temperature (K)	$\chi^2_{\min}$/dof at orbital phase: 0.5	0.96
HD 77818	4777 ± 60	1.47	1.35
HD 95526	4832 ± 60	1.36	1.28
HD 31451	4921 ± 60	1.27	1.20
HD 40537	4962 ± 60	1.33	1.24
HD 122253	5007 ± 60	1.24	1.19
HD 14855	5023 ± 60	1.24	1.15
HD 17620	5159 ± 60	1.24	1.21
HD 108189	5373 ± 60	1.35	1.40

3.3 Binary mass ratio

The donor-to-WD mass ratio ($q = M_2/M_1$) is related to K_2 and $v_{\rm rot} \sin i$ through:

$$v_{\rm rot} \sin i \simeq 0.49(1+q)q^{2/3} K_2 \left[0.6 q^{2/3} + \ln(1 + q^{1/3}) \right]^{-1} . \quad (2)$$

This relation is obtained adopting the Eggleton's approximation for the Roche lobe radius (Eggleton 1983) and under the assumptions that the orbit of the system is circular, the angular momentum vector of both the orbit and the donor star are aligned and that their rotation is synchronized as a result of tidal interactions. Hence, q can be derived from K_2 and $v_{\rm rot} \sin i$. The latter is provided by the subtraction of stellar templates described in Section 3.2. Here we apply this technique to all our spectra in the same wavelength range as used in the radial velocity analysis (Section 3.1) with the HD 20165 and HR 2556 spectral templates. The templates were observed with the same instrumental setup as the target, except for the WHT/ISIS R600R data. In this case, we used the WHT/ISIS R1200R templates smoothed with a Gaussian profile to match the spectral resolution. Fig. 2 displays the normalised, Doppler-shifted average of GK Per before and after the subtraction of the broadened K1 V template.

Evaluation of the uncertainties for $v_{\rm rot} \sin i$ and f was performed by Monte Carlo randomization following the approach in Steeghs & Jonker (2007) and Torres et al. (2020). The optimal subtraction procedure was repeated for 10000 bootstrapped copies of the GK Per average spectrum. This delivered the distributions of possible values for $v_{\rm rot} \sin i$ and f, which are well fitted by Gaussians. Hence, we took their mean and standard deviation as the value and 1-σ uncertainty,
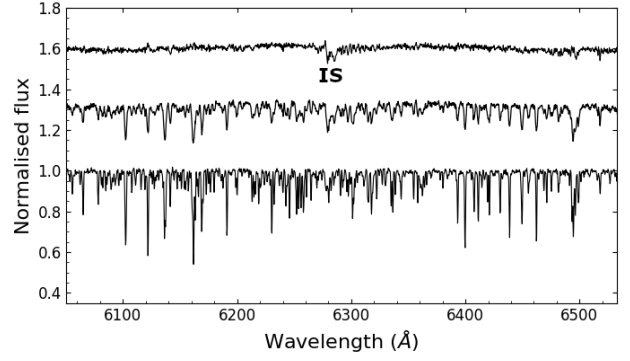

Figure 2. Result of the optimal subtraction technique to measure $v_{\rm rot} \sin i$ and f from the WHT/ISIS spectra taken on 2018 December 1. From bottom to top: spectrum of the K1 V template HD 20165, the average spectrum of GK Per in the rest frame of the donor star and the residual spectrum after subtraction of the broadened and scaled template. The spectra have been shifted vertically for display purposes. "IS" marks an interstellar absorption band contaminated with telluric absorption.

respectively (Table 6). The rotational velocities obtained from the NOT, HCT and Xinglong spectra are overestimated and/or have large uncertainties as a result of the lower spectral resolution ($\simeq 170 - 270$ km s^{-1}; see Table 1). The spectral resolution of the WHT/ISIS R600R data is comparable to the $v_{\rm rot} \sin i$ of the system, but the templates were not obtained with the same instrumental setup. For these reasons, only the measurements of $v_{\rm rot} \sin i$ from the WHT/ISIS R1200R data will be considered.

The observed variability of $v_{\rm rot} \sin i$ with the orbital phase (see Table 6) may be compatible with that expected for a Roche lobe-filling donor star (see e.g. Shahbaz et al. 2014). However, our sampling is insufficient to establish the phase dependence of $v_{\rm rot} \sin i$: only critical orbital phases were covered to estimate its mean value. Taking the averages at phases $\approx$ 0.0, 0.5 and 0.7 we derive $v_{\rm rot} \sin i = 51 \pm 2$ km s^{-1} and $v_{\rm rot} \sin i = 54 \pm 2$ km s^{-1} for HD 20165 and HR 2556, respectively. Given that the minimum χ^2 value of the optimal subtraction is similar for both templates, we adopt the mean $v_{\rm rot} \sin i = 52 \pm 2$ km s^{-1}. Our result is a significant improvement on the previous estimates of 61.5 ± 11.8 km s^{-1} (MR02) and 55 ± 10 km s^{-1} (Harrison & Hamilton 2015).

We derived q using Eq. 2 and $v_{\rm rot} \sin i$ and K_2 (Section 3.1). To compute its uncertainty, we followed a Monte Carlo approach: we picked random values of K_2 and $v_{\rm rot} \sin i$ from normal distributions defined by the mean and the 1-σ uncertainties of our measurements. We then calculated q for each random set of parameters and repeated this process 10000 times. The resulting values of q also followed a normal distribution and hence we took the mean and the standard deviation as reliable estimates of its value and uncertainty, respectively. We finally obtain a binary mass ratio:

$$q = 0.38 \pm 0.03 .$$

MR02 reported a highly uncertain $q = 0.55 \pm 0.21$ using the same technique with lower resolution B-band spectra. Crampton et al. (1986) estimated $q = 0.28 \pm 0.04$ from the quotient of the donor and the Hβ radial velocity semi-amplitudes. This discrepancy indicates that the Hβ emission line is indeed not a good tracer of the WD motion, as pointed out by MR02.

Table 6. $v_{rot} \sin i$ and f from the optimal subtraction of the HD 20165 (K1 V) and HR 2556 (K0 III-IV, in brackets) template spectra. The * marks the WHT/ISIS R1200R observations, that provided robust measurements of $v_{rot} \sin i$.

Telescope Date	Mean orbital phase	$v_{rot} \sin i$ (km s^{-1})	f
HCT			
2017 Dec 06	0.26	72 ± 10	0.67 ± 0.02
		(85 ± 10)	(0.73 ± 0.02)
2017 Dec 07	0.76	72 ± 8	0.69 ± 0.02
		(85 ± 9)	(0.75 ± 0.02)
2017 Dec 08	0.26	64 ± 9	0.69 ± 0.02
		(81 ± 8)	(0.75 ± 0.02)
NOT			
2017 Dec 08	0.39	65 ± 5	0.66 ± 0.01
		(72 ± 5)	(0.74 ± 0.02)
2017 Dec 09	0.92	63 ± 5	0.69 ± 0.02
		(65 ± 5)	(0.79 ± 0.01)
2017 Dec 10	0.40	66 ± 5	0.70 ± 0.01
		(76 ± 5)	(0.79 ± 0.02)
WHT			
2018 Dec 01*	0.70	53.8 ± 0.7	0.71 ± 0.01
		(56.1 ± 0.8)	(0.77 ± 0.01)
2019 Aug 24	0.00	48 ± 3	0.61 ± 0.02
		(53 ± 3)	(0.70 ± 0.02)
2019 Aug 25	0.48	45 ± 2	0.61 ± 0.01
		(48 ± 2)	(0.70 ± 0.01)
2019 Sep 7*	0.98	48.5 ± 0.5	0.71 ± 0.01
		(50.8 ± 0.6)	(0.78 ± 0.01)
2019 Sep 8*	0.50	50.5 ± 0.8	0.67 ± 0.01
		(51.7 ± 0.9)	(0.72 ± 0.02)
2019 Sep 12*	0.50	52.6 ± 0.5	0.59 ± 0.01
		(53.8 ± 0.5)	(0.65 ± 0.01)
2019 Sep 13*	0.96	48.1 ± 0.6	0.65 ± 0.01
		(50.7 ± 0.6)	(0.71 ± 0.01)
2.16m-Xinglong			
2019 Nov 14	0.74	79 ± 7	0.60 ± 0.01
		(82 ± 8)	(0.64 ± 0.02)

3.4 Ellipsoidal light curve and orbital inclination

In this section we model the *R*-band light curve of GK Per. We start by detailing the steps followed to obtain an ellipsoidal light curve as free as possible from night-to-night variations due to accretion. Then, we present and discuss the light curve modelling and provide the binary inclination.

3.4.1 Multi-epoch R-band light curve

We constructed the phase-folded *R*-band light curve of GK Per using the photometry data described in Section 2.2 (see Table 2) and the ephemeris obtained in Section 3.1. In order to exclude the data points affected by large systematic errors we examined the flux stability of the GK Per-10 check star relative to the GK Per-12 comparison star (see Section 2.3). After some testing, we removed the points with a relative deviation > 0.03 mag from the mean. Similarly, points with a statistical uncertainty > 0.03 mag were also removed. The bottom panel of Fig. 3 shows the final GK Per-10/GK Per-12 relative flux curve.

The cleaned, phase-folded *R*-band light curve of GK Per (top panel of Fig. 3) shows clear night-to-night variations likely due to changes in the light contribution of the accretion flow. To correct for these, we took advantage of the partially simultaneous photometry and spectroscopy on 2017 December 7–10. The photometry yielded flux points that cover the orbital phases $0.2 − 0.5$ and $0.65 − 0.95$, while the spectra provided a nearly constant f for those nights (see Table 6). The correction consisted of adding or subtracting a constant value to shift the photometry data of all the other nights to match the flux of the above four reference nights. This was accomplished in three steps: first, the light curves that cover the same orbital phases as the reference nights were shifted to the mean reference flux level in the range of coincidence. The resulting light curve is shown in panel B of Fig. 3. Second, we applied the flux shifts obtained in the previous step to the light curves that sample different orbital phases during the same nights. By doing this, we are assuming that the variability is negligible for time intervals shorter than one day. Finally, the remaining observations were offset to match the mean relative flux of the data points corrected in the second step. The resulting *R*-band light curve is shown in panel C of Fig. 3. Given the steps followed above, the value of the fractional contribution of the donor star to the total flux in the light curve should match that obtained from the spectroscopy on the reference nights ($f = 0.66 − 0.70$ or $0.73 − 0.79$, depending on the template; see Table 6). After the above corrections, the ellipsoidal modulation becomes apparent in the light curve with a peak-to-peak amplitude of ≈ 0.25 mag.

We also constructed the phase-folded *TESS* light curve (Section 2.2.5) using our ephemeris. We only combined six out of a total of eight full orbital cycles since the system appeared to be increasing in brightness during the first two. Prior to phase-folding, we flux-shifted the data corresponding to individual full orbital cycles in order to have all of them with a common mean flux level.

Figure 4 shows the *R*-band (top panel) and the *TESS* (bottom panel) light curves of GK Per after applying a 0.01-phase binning and dividing them by their mean flux. While the former shows maxima consistent with being identical in amplitude, the *TESS* light curve hints to unequal maxima. Hence multi-colour photometry with good coverage of the full orbit will allow to check for this behaviour, which might be related to a disc hot spot and/or a spotted donor star. On the other hand, the phase-folded *R*-band photometry deviates from the expected ellipsoidal modulation at phases $0.0 − 0.1$ and the slope of the individual *R*-band light curves in that phase range shows significant night-to-night variation (see panels A to C of Fig. 3). For this reason we decided to exclude the $0.0 − 0.1$ orbital phase range from the modelling.
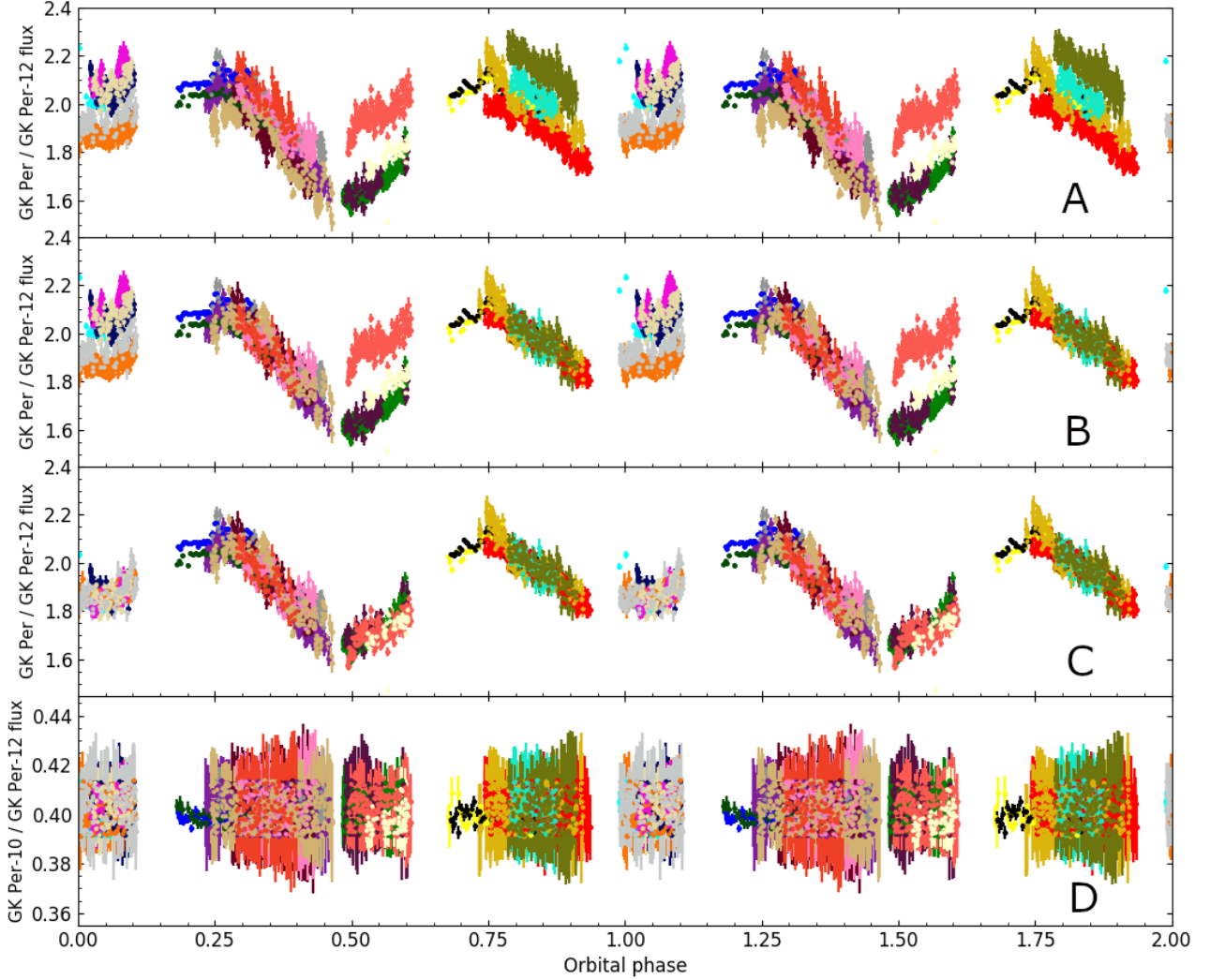
Figure 3. Construction of the phase-folded *R*-band light curve of GK Per. Panels A to C illustrate the steps followed to correct the photometry for night-to-night accretion variability, while panel D displays the flux of the GK Per-10 check star relative to the GK Per-12 comparison star. Panel A shows the light curve prior to applying any variability correction. Panel B displays the light curve after shifting the relative flux of the data points that cover similar orbital phases than the 2017 December 7–10 photometry. The shifts are applied in order to match the mean flux measured during those above nights. Panel C shows the result after correcting the flux points at other orbital phases. Each colour in the plot represents a different night. See text for more detail. Two cycles are shown for the sake of clarity.

3.4.2 Light curve modelling

We modelled the *R*-band light curve by fitting synthetic light curves generated with XRBINARY, a code developed by E. L. Robinson[8]. It accounts for the photometric modulation of a binary system composed of a primary star (assumed to be a point source) surrounded by an accretion disc and a co-rotating Roche lobe-(fully) filling donor star. The disc can be non-axisymmetric and vertically extended. The code also allows for an outer disc rim, an inner torus and disc spots of different brightness. The flux spectrum of the donor star is computed from the stellar atmosphere models of Kurucz (1996) using a non-linear limb-darkening law (Claret 2000b) valid for log *g* = 0.0 − 5.0 dex. The gravity darkening only depends on the star's effective temperature and is based on Claret (2000a). The

accretion disc is assumed to be optically thick and to emit as a multi-temperature blackbody. The disc temperature radial profile is given by $T = K r^\beta$, where K is a normalisation constant and r is the distance to the primary star (see the XRBINARY manual for further details). Other accretion structures and the primary star are also assumed to emit as black bodies. Ray tracing is used to compute the light curve, that can be generated for the Johnson-Cousins filters or for square bandpasses (Bayless et al. 2010).

The disc opening angle can be estimated as $\alpha \simeq 2 \arctan[0.038(\dot{M}/10^{16})^{3/20}]$ (Warner 1995). Following Webbink et al. (1987) and Anupama & Prabhu (1993) we calculated an accretion rate in the disc $\dot{M} = (1.0–3.8) \times 10^{17}$ g s^{-1} for orbital inclinations and WD masses in the ranges $55° − 72°$ and $0.8 − 1.2\,M_\odot$, respectively. On the other hand, Bianchini & Sabbadin (1983) and Wada et al. (2018) presented values very close to $\dot{M} \simeq 10^{16}$ g s^{-1}. Considering the accretion rate to be in the range $\dot{M} \simeq 10^{16} − 10^{17}$ g s^{-1}, we obtain $\alpha \approx 4° − 6°$. For the light curve modelling we adopted

8 A detailed description of XRBINARY can be found at: http://www.as.utexas.edu/~elr/Robinson/XRbinary.pdf
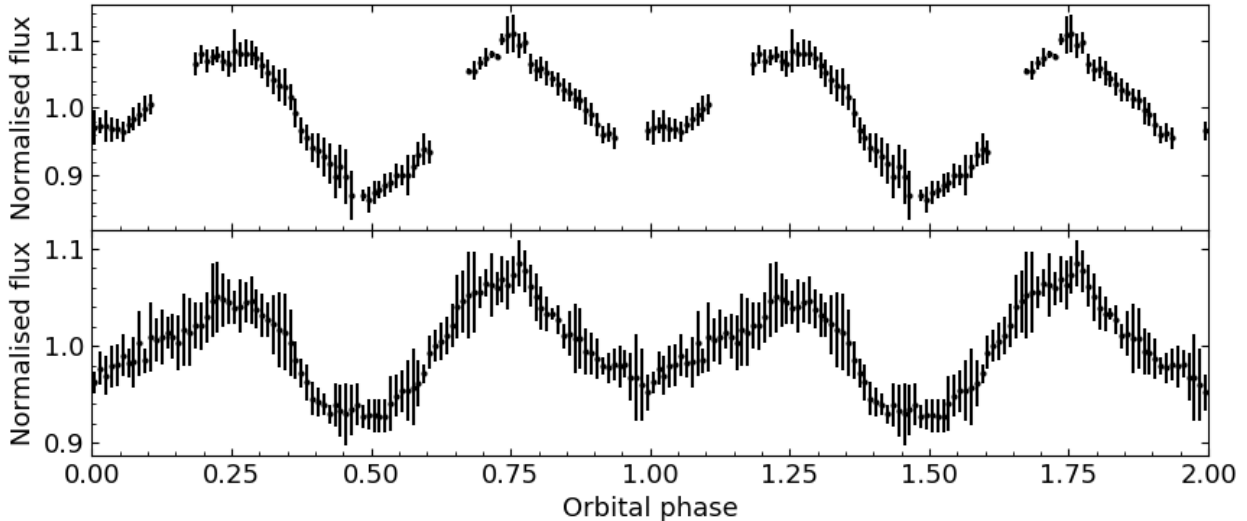
Figure 4. Top panel: Phase-folded R-band light curve of GK Per after correcting for night-to-night accretion variability. Bottom panel: *TESS* light curve obtained by phase folding six orbital cycles scaled to have the same mean flux. A 0.01-phase binning has been applied to both data sets.

the upper limit, although using a flat disc ($\alpha \simeq 0°$) produces the same results. We also assumed a circular disc extending up to the circularisation radius $R_c = (1 + q)(b_1/a)^4$, where b_1 is the distance from the primary star to the inner Lagrangian point of the system, with $b_1/a = (1.0015 + q^{0.4056})^{-1}$ (Warner 1995).

We fixed the donor star effective temperature (T_2) at 5000 K following the spectroscopic measurement by Harrison (2016), which is supported by our analysis in Section 3.2. We did not include either a disc hot spot or donor star spots given that the R-band light curve has its two maxima at the same flux level within the errors. In addition, we could not place constrains on the temperature of the disc outer edge or the albedos of the donor star and the disc. However, we checked that these parameters have a negligible impact on the light curve modelling and we fixed them at 2000 K and 0.5, respectively. The free parameters in our model are the orbital inclination (i), the bolometric luminosity of the disc (L_D), the exponent of the disc temperature radial profile (β), the disc inner radius (R_{in}), q and K_2.

We used the Markov chain Monte Carlo (MCMC) EMCEE[9] package (Foreman-Mackey et al. 2013) in PYTHON along with wide uniform uninformative priors for β and R_{in}. The prior for L_D was flat in log space to allow for an even sampling of the parameter space across orders of magnitude. The absence of eclipses in GK Per (Reinsch 1994) implies $i \lesssim 73°$ (MR02) and the Chandrasekhar mass limit for a WD imposes $i \gtrsim 55°$. We used a flat prior for $\cos i$ and conservatively adopted a $50° - 85°$ range. We adopted Gaussian priors for K_2 and q, with the mean and standard deviation values obtained in Sections 3.1 and 3.3, respectively. We ran the MCMC sampler for 10000 steps with 40 walkers and discarded the first 50 per cent as burn-in. In each iteration, the comparison between the synthetic and the actual R-band light curves is based on the likelihood function of a continuous distribution, computed after normalizing the synthetic light curve to be at the same flux level as the observed one. After several trials we mostly found flat/wide posteriors for R_{in} and β, so we were unable to constrain them. Therefore, we decided to marginalise

over these two parameters and provide the correlation plot (Fig. 5) for the remaining parameters and the inferred ones (M_1 and M_2), whose posterior distributions are close to normal. Table 7 provides the fixed and the fitted model parameters, with the quoted uncertainties established from the 68th percentiles in the distributions.

The best-fit model light curve ($\chi^2/\text{dof} = 0.6$) is presented in the top panel of Fig. 6 as a solid line. It provided a donor star fractional contribution to the R-band flux $f = 0.73 \pm 0.02$, in agreement with what we found from the spectroscopy using the K0 III-IV template on the 2017 December 7–10 data (see Section 3.3). This template has an effective temperature of 5056 ± 111 K, fully consistent with the T_2 adopted in the model, and $\log g = 3.08 \pm 0.06$ dex (Jönsson et al. 2020). The MCMC analysis yields an orbital inclination of $i = 67° \pm 5°$. In Fig. 6 we show two synthetic light curves computed using the best-fit parameters and the above inclination limits of $55°$ and $73°$ (dotted and dashed lines, respectively). The $82° - 86°$ binary inclination obtained by Kim et al. (1992) from modelling of the dwarf nova outbursts can be rejected, while the estimate of $66°$ reported in Bianchini et al. (1982) is in line with our measurement. From our value of the orbital inclination we derive the following binary masses:

$$M_1 = 1.03^{+0.16}_{-0.11} \, M_\odot , \qquad\qquad M_2 = 0.39^{+0.07}_{-0.06} \, M_\odot .$$

The lack of data points around phase 0 in our R-band light curve does not allow us to firmly discard disc eclipses. However, the *TESS* light curve suggests that they are either too shallow to be detected or absent. We have computed R-band synthetic light curves and have assumed that the eclipse depth is the same in both the *TESS* and the R bands. Disc eclipses deep enough to be noticeable in the *TESS* light curve would then be produced for $i \gtrsim 71°$. Thus, the binary inclination is most likely $i \lesssim 71°$, which means that our upper limit on the uncertainty in i is overestimated by $1°$. In turn, this leads to a negligible overestimate of $0.01 \, M_\odot$ for the lower limit on M_1. Another source of systematic errors in the masses is a potential incorrect determination of the relative contribution of the donor star and the accretion flow to the R-band flux. Using the optimal subtraction technique (Section 3.3) we determined $f \simeq 0.66 - 0.70$ or

[9] https://emcee.readthedocs.io/en/stable/

Table 7. Fixed and fitted parameters of the R-band light curve modelling. The type of prior for each parameter was: flat for β and $R_{\rm in}$, flat in log space for L_D, flat in cosine space for i and Gaussian for K_2 and q (based on the results presented in Sections 3.1 and 3.3).

Parameter	Prior	Best-fit value
P (d)	Fixed	1.996872
α (°)	Fixed	6
T_2 (K)	Fixed	5000
Disc albedo	Fixed	0.5
Donor albedo	Fixed	0.5
i (°)	[50, 85]	67 ± 5
$\log(L_{\rm D})$ (erg s^{-1})	[33, 35.5]	33.8 ± 0.3
q	0.38 ± 0.03	0.38 ± 0.03
K_2 (km s^{-1})	126.4 ± 0.9	126.4 ± 0.9
β	[-3.0, 3.0]	–
$R_{\rm in}/a$	[0.001, 0.2]	–

$f \simeq 0.73 - 0.79$ depending on the template, while the best-fit light curve model yields $f = 0.73$. Modifying the phase-folded data to simulate light curves with $f = 0.65$ and $f = 0.8$ results in $i = 66°^{+4°}_{-5°}$ and $i = 68° \pm 4°$, respectively. These changes in the inclination have an impact on the derived masses lower than the reported statistical uncertainties. Finally, we have also tested the systematic errors associated to the adopted T_2. Fixing the temperature of the donor at either $T_2 = 4700$ K or $T_2 = 5300$ K results in an orbital inclination of $i = 68°^{+4°}_{-5°}$ and $i = 66°^{+6°}_{-5°}$, respectively. Thus, even considering these less probable values for T_2, its effect on the dynamical masses is significantly lower than the statistical uncertainties.

4 DISCUSSION

4.1 Binary masses

The mass and radius of the Roche-lobe filling donor in GK Per are $M_2 = 0.39^{+0.07}_{-0.06}$ M$_\odot$ and $R_2 = \frac{P}{2\pi} \frac{v_{\rm rot} \sin i}{\sin i} = 2.26 \pm 0.12$ R$_\odot$, respectively, which clearly indicates that the donor star is evolved. In fact, we derive $\log g = 3.31 \pm 0.09$ dex, which differs from $\log g = 4.0$ dex adopted by Harrison (2016) to measure a donor effective temperature $T_2 = 5000$ K and a metallicity [Fe/H] $= -0.3$ dex from synthetic template spectra. However, our spectral clasification using empirical subgiant templates in the range $\log g = 3 - 3.6$ dex provides a very similar temperature of $\simeq 4900 - 5150$ K. The above value for T_2 is also supported by observations of evolved field stars with $\log g \simeq 3.2 - 3.4$ dex and metallicities from -0.2 to -0.4 dex that have effective temperatures of $4900 - 5100$ K (Alves et al. 2015). On the other hand, if the donor star were a stripped giant with all its properties dependent on the mass of its helium core, we could derive its effective temperature from R_2. Following the equations given in Webbink et al. (1983) and King (1988) we obtained a core mass 0.179 ± 0.002 M$_\odot$, a luminosity 2.16 ± 0.19 L$_\odot$ and $T_2 = 4660 \pm 26$ K. This lower T_2 could be an indication that the donor star in GK Per is not a stripped giant as initially suggested by Watson et al. (1985). This would imply that its initial mass was $\lesssim 1.4$ M$_\odot$ (Ziółkowski & Zdziarski 2020).

Our dynamical study of GK Per has also provided a WD mass $M_1 = 1.03^{+0.16}_{-0.11}$ M$_\odot$. Zorotovic et al. (2011) found an average mass

of 0.83 ± 0.23 M$_\odot$ from robust measurements in 32 CVs. This value is significantly higher than the mean of $\approx 0.61 - 0.64$ M$_\odot$ established for isolated WDs (Kepler et al. 2016). The WD mass in GK Per is no exception — it is among the ten more massive ones in Zorotovic et al.'s sample.

4.2 Comparison with previous WD mass estimates

Hachisu & Kato (2007, see also Hachisu & Kato 2015) fitted the 1901 to 1919 decay light curve of the nova event. They adopted the model described in Hachisu & Kato (2006) that uses a decay law for the optical flux, $F_\lambda \propto t^{-\alpha}$, and considers a spherical ejecta whose optical-to-infrared continuum flux is dominated by free-free emission from the optically thin region. They model the different stages of the flux decay using a sequence of steady-state solutions and find that the decline rate depends weakly on the chemical composition and is very sensitive to the WD mass. They provided a WD mass (hereinafter $M_1^{\rm nova}$) as a function of the hydrogen content of the ejecta, X, as $M_1^{\rm nova}(X) \simeq M_1^{\rm nova}(X = 0.55) + 0.5(X - 0.55)$, valid for $0.35 \leq X \leq 0.65$ and where $M_1^{\rm nova}(X = 0.55) = 1.15 \pm 0.05$ M$_\odot$. Note that according to Pottasch (1959) the hydrogen content of the nova ejecta in GK Per is $X \simeq 0.54$. The WD mass obtained from the nova light curve agrees within 1-σ of our dynamical measurement.

More recently, Shara et al. (2018) interpolated the grid of nova models from Yaron et al. (2005) to construct functions for the WD mass and the accretion rate depending on the flux amplitude and the mass-loss time of a given nova. Assuming that the latter is equal to the decline time and fitting these functions to the light curve of Nova Persei 1901 they derived $M_1^{\rm nova} = 1.22$ M$_\odot$ with an estimated statistical uncertainty of ~ 0.1 M$_\odot$. Our dynamical measurement is also in agreement within 1-σ of this value.

Attempts to derive the WD mass from modelling of X-ray data (hereinafter $M_1^{\rm X}$) have been reported by different authors. The simplest X-ray models for IPs assume that the accreted matter falls almost radially onto the WD from infinity. Hence, the temperature of the plasma in the post-shock region, T_s, may reflect the depth of the gravitational potential of the WD (Aizu 1973):

$$kT_s = \frac{3}{8} \frac{GM_1^{\rm X}}{R_1} \mu m_{\rm H} = 16 \left(\frac{M_1^{\rm X}}{0.5 \, {\rm M_\odot}} \right) \left(\frac{R_1}{10^9 \, {\rm cm}} \right) \, ({\rm keV}) , \quad (3)$$

where R_1 is the radius of the WD, μ is the mean molecular weight (= 0.615 for solar abundance plasma) and $m_{\rm H}$ is the mass of the hydrogen atom. Given that R_1 can be expressed as a function of the WD mass using a mass-radius relation (e.g. Nauenberg 1972), the temperature can be expressed as a function of the WD mass only. The hot post-shock region cools mainly via thermal bremsstrahlung emission in the hard X-ray regime. Hence, the easiest way to estimate the plasma temperature and thus derive the WD mass is to fit the hard X-ray spectra with single-temperature bremsstrahlung models and adopt the best-fit temperature as the maximum shock temperature.

Landi et al. (2009) fitted the combined $0.2 - 10$ keV *Swift*/XRT and $20 - 100$ keV *INTEGRAL*/IBIS spectrum of GK Per with a blackbody plus bremsstrahlung model for the soft and hard X-ray emission, respectively, taking into account the local and interstellar absorption. The best-fit bremsstrahlung temperature $kT_s = 23^{+9.2}_{-6.5}$ keV yields (Equation 3) $M_1^{\rm X} = 0.87^{+0.25}_{-0.21}$ M$_\odot$ (Brunschweiger et al. 2009). Given its large uncertainty this mass estimate agrees within 1-σ of our dynamical measurement.

Other authors have considered a multi-temperature continuum post-shock region. Suleimanov et al. (2005) presented a model with
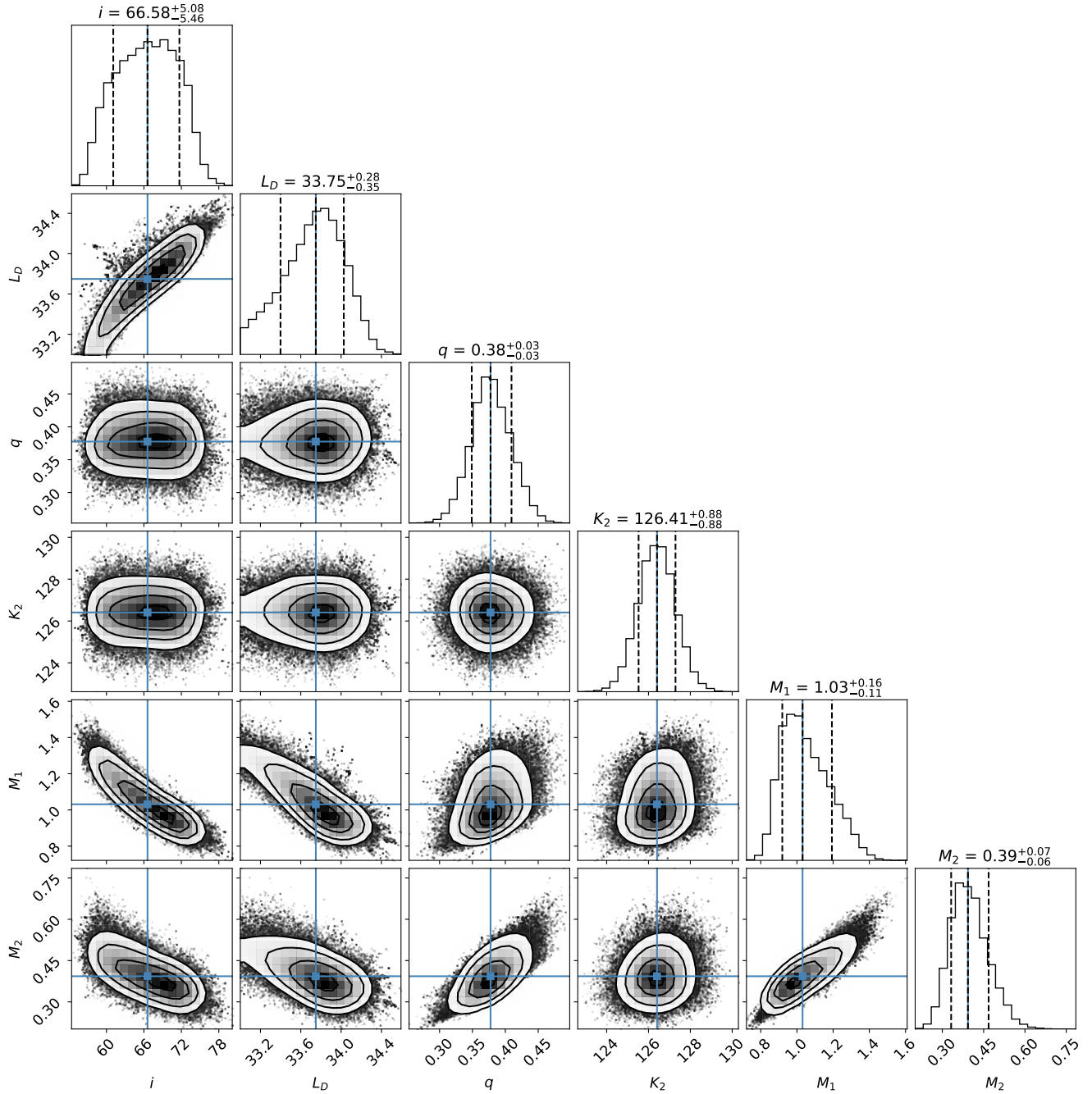
Figure 5. Correlation diagrams of the probability distributions of the best-fit parameters from the MCMC modelling of the ellipsoidal light curve. The contours in the 2D plots show the 68, 95 and 99.7 per cent confidence regions. The right panels show the projected 1D distributions of the parameters, where we mark the mean (solid line) and 68 per cent confidence level intervals (dashed lines). M_1 and M_2 are inferred values from q, K_2, P and i.

temperature and density as functions of the distance to the WD surface under the assumption that matter is accreted from infinity. The latter is a good approximation when the Alfvén radius (R_A) is more than 10 times larger than the WD radius. They fitted this model to a $3 - 100$ keV outburst spectrum of GK Per obtained by combining *RXTE* PCA and *HEXTE* data and found a much lower WD mass of $M_1^X = 0.59 \pm 0.05 \, M_\odot$. Given that $R_A/R_1 < 5$ when GK Per is in outburst and $R_A/R_1 < 10$ during quiescence, Suleimanov et al. (2005) concluded that their value of M_1^X obtained from outburst data

underestimated the WD mass by at least 20 per cent. Our dynamical mass measurement allows to establish that their M_1^X actually underestimates the WD mass by 73^{+40}_{-17} per cent. These authors also fitted their models to the $3 - 20$ keV PCA data alone and obtained $M_1^X = 1.24 \pm 0.10 \, M_\odot$. They showed that the use of the X-ray continuum in the energy range < 20 keV does not provide an accurate estimate of M_1 because for WD masses $> 0.6 \, M_\odot$ the post-shock temperature is > 20 keV. Further, the IP X-ray continuum in that range is affected by interstellar and intrinsic absorption and possibly
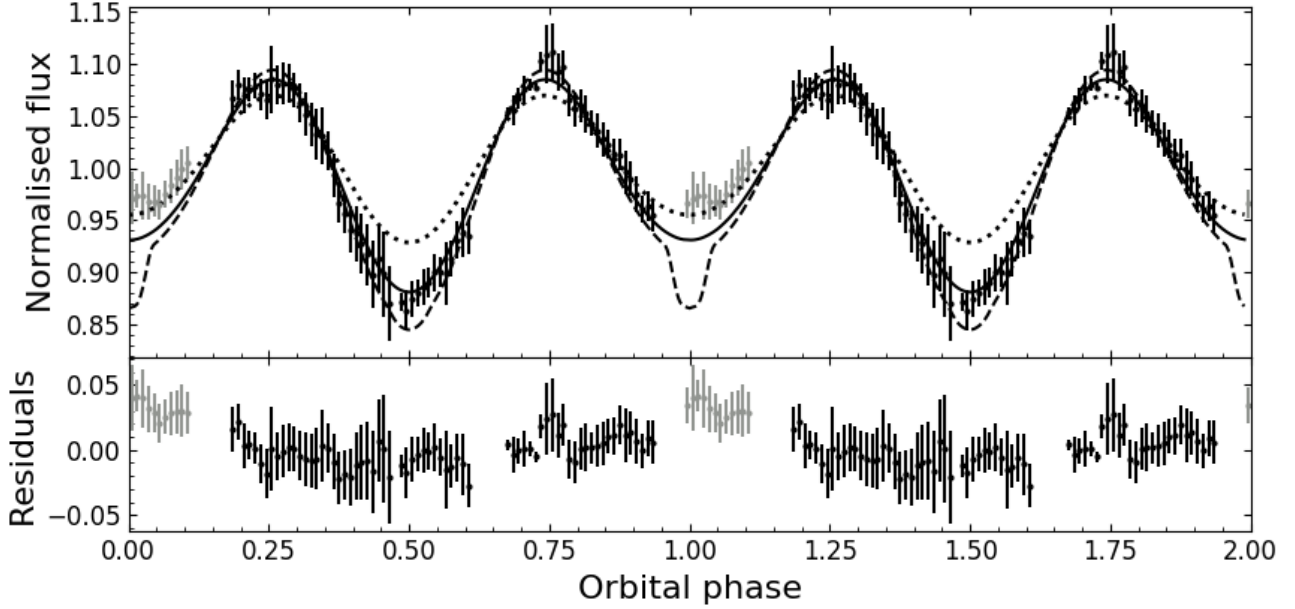
Figure 6. Top panel: Phase-folded *R*-band light curve and the best-fit synthetic model (solid black line). The points in grey colour (phases $0.0 - 0.1$) have been masked during the fit. The flux of the accretion disc (not shown) in the model is constant along the whole orbit, while the fractional contribution of the donor star to the relative flux is $f = 0.73 \pm 0.02$. The dashed and dotted black lines represent the synthetic light curves for $i = 73°$ and $i = 55°$, respectively. Bottom panel: Residuals from the fit.

a reflection component. In this regard, Evans & Hellier (2007) fitted the multi-temperature continuum model for the post-shock region by Cropper et al. (1999), which is similar to that in Suleimanov et al. (2005), to a $0.2 - 12$ keV *XMM-Newton*/EPIC-pn spectrum of GK Per in outburst. The fit provided $M_1^X = 0.92^{+0.39}_{-0.13}\,\mathrm{M_\odot}$, which agrees with our measurement given the large uncertainties.

The systematic underestimate of the WD mass of GK Per as a function of its accretion state was explored by Brunschweiger et al. (2009). They fitted the Suleimanov et al. model to both quiescence and outburst $15 - 200$ keV *Swift*/BAT spectra. For the outburst data they derived a mass $M_1^X = 0.67 - 0.74\,\mathrm{M_\odot}$ lower than the result in quiescence $M_1^X = 0.90 \pm 0.12\,\mathrm{M_\odot}$. They suggested a true WD mass of $1.15\,\mathrm{M_\odot}$ from fitting the relation between M_1^X and the accretion rate of the system when the data are taken. This value is in line with our result.

In order to determine a M_1^X free of this underestimate effect, Suleimanov et al. (2016) proposed a method that obtains M_1^X and R_A simultaneously from the break frequency of the power spectrum[10] and a model with the matter falling from R_A, not from infinity. By fitting this refined model to a $20 - 80$ keV *NuSTAR* spectrum of GK Per in outburst they found $M_1^X = 0.86 \pm 0.02\,\mathrm{M_\odot}$ and $R_A/R_1 = 2.8 \pm 0.2$. This same method was applied to a $20 - 80$ keV *NuSTAR* spectrum taken in quiescence (Suleimanov et al. 2019) that provided $M_1^X = 0.79 \pm 0.01\,\mathrm{M_\odot}$ and $R_A/R_1 = 3.18 \pm 0.17$. These M_1^X values are consistent within $2-\sigma$ of the dynamical WD mass presented in this work.

Other methods have been explored to derive the WD mass in

GK Per using X-ray data. Ezuka & Ishida (1999) fitted the continuum emission of a $0.5 - 10$ keV spectrum of GK Per in outburst combining *ASCA*/SIS and GIS data. Their model consists of single-temperature thermal bremsstrahlung that undergoes multi-column absorption. This included the fluorescent (6.4 keV) and plasma (6.7 and 7.0 keV) components of the iron Kα emission line. They used the intensity ratios of these lines to measure the ionisation temperature and obtained $kT = 7.8^{+2.1}_{-1.8}$ keV. They also derived a relation between this and the corrected temperature of the continuum (see panel *b* of fig. 4 in Ezuka & Ishida 1999). This yields $M_1^X = 0.52^{+0.34}_{-0.16}\,\mathrm{M_\odot}$ (90 per cent confidence level). The discrepancy with our $1.03^{+0.16}_{-0.11}\,\mathrm{M_\odot}$ dynamical value shows that the above temperature relation must be improved in order to obtain reliable WD masses. Finally, Wada et al. (2018) derived a M_1^X–R_A relation for a given temperature of the post-shock region by modifying Equation 3 to account for the free-fall initial point and the shock height. They fitted a multi-temperature optically-thin plasma model to the quiescence and outburst *NuSTAR* spectra analysed in Suleimanov et al. (2016, 2019). From the flux and plasma temperature measured at different accretion states they established that R_A in quiescence is 3.9 times larger than during outburst. By finding the M_1^X value that satisfies this condition they derived $0.87 \pm 0.08\,\mathrm{M_\odot}$, which is consistent within 1-σ of our dynamical mass.

5 CONCLUSIONS

We have presented a dynamical study of the intermediate polar cataclysmic variable GK Per 120 years after its nova explosion. We obtained the radial velocity curve of the donor star and refined the orbital period of the system to 1.996872 ± 0.000009 d and K_2 to $126.4 \pm 0.9\,\mathrm{km\,s^{-1}}$. From our higher resolution spectroscopy we established a rotational broadening for the donor star absorption lines $v_{\mathrm{rot}} \sin i = 52 \pm 2\,\mathrm{km\,s^{-1}}$. Partially simultaneous photometry

---

[10] The power spectra of X-ray pulsars and IPs exhibit a break at the frequency of the Keplerian rotation at the boundary of the magnetosphere (Revnivtsev et al. 2009, 2011).

Table 8. Fundamental parameters of GK Per obtained in this work.

Parameter	Value
P (d)	1.996872 ± 0.000009
K_2 (km s^{-1})	126.4 ± 0.9
$v_{\rm rot} \sin i$ (km s^{-1})	52 ± 2
q	0.38 ± 0.03
i (°)	67 ± 5
M_1 (M$_\odot$)	$1.03^{+0.16}_{-0.11}$
M_2 (M$_\odot$)	$0.39^{+0.07}_{-0.06}$
R_2 (R$_\odot$)	2.26 ± 0.11

and spectroscopy allowed us to construct a phase-folded *R*-band light curve as free as possible from night-to-night accretion variability. Modelling of the light curve allowed to establish the binary orbital inclination $i = 67 \pm 5°$. We derived the dynamical masses $1.03^{+0.16}_{-0.11}$ M$_\odot$ and $0.39^{+0.07}_{-0.06}$ M$_\odot$ for the WD and the evolved donor star, respectively.

The WD in GK Per has one of the highest masses confirmed dynamically for a CV and our value is in agreement with those obtained from modelling of the nova decay light curve. We also compared the WD mass with X-ray modelling estimates. We confirm that the WD mass values derived from the hard X-ray spectra (> 20 keV) continuum temperature assuming matter free falling from infinity are significantly underestimated. Models considering gas free falling from a finite distance (Suleimanov et al. 2016, 2019) agree with our measurement within 2-σ. The same degree of agreement is found for the estimates obtained from the intensity ratio of the fluorescent and plasma components of the Kα emission line (Ezuka & Ishida 1999). On the other hand, the WD mass value obtained by Wada et al. (2018) using the quiescence-to-outburst Alfvén radius ratio is consistent within 1-σ of our dynamical measurement.

Our robust dynamical mass for the WD in GK Per has served as a stringent test for the values reported by other authors using indirect methods. However, a more accurate M_1 is still needed to further constrain the nova decay light curve and X-ray spectral modelling techniques. Future multi-colour photometry sampling the full binary orbit will likely result in a more precise value of the inclination that could potentially lead to a refined dynamical WD mass.

Finally, our study supports a subgiant donor with an effective temperature of $\simeq$ 5000 K, in line with the values obtained from infrared spectroscopy by Harrison et al. (2013) and Harrison (2016). The stripped giant model failed to explain the observed temperature, which suggests that the initial mass of the donor star was $\lesssim 1.4$ M$_\odot$.

DATA AVAILABILITY

The NOT and WHT data are available at `http://www.not.iac.es/observing/forms/fitsarchive/` and `http://casu.ast.cam.ac.uk/casuadc/ingarch/query`, respectively. They can be searched by observing date and object coordinates. The 0.3-m SC30, 0.43-m CDK, 0.4-m UOAO and 2.16-m Xinglong data are available from the corresponding author on request. The HCT and 1.3-m JCBT data will be made available by G. C. Anupama and M. Pavana on request.

REFERENCES

Aizu K., 1973, Progress of Theoretical Physics, 49, 1184
Alves S., et al., 2015, MNRAS, 448, 2749
Anupama G. C., Kantharia N. G., 2005, A&A, 435, 167
Anupama G. C., Prabhu T. P., 1993, MNRAS, 263, 335
Bayless A. J., Robinson E. L., Hynes R. I., Ashcraft T. A., Cornell M. E., 2010, ApJ, 709, 251
Bianchini A., Sabbadin F., 1983, The continuum energy distribution of the old-nova GK Per (1901). pp 127–130, doi:10.1007/978-94-009-7118-9_15
Bianchini A., Sabbadin F., Hamzaoglu E., 1982, A&A, 106, 176
Bode M. F., Seaquist E. R., Frail D. A., Roberts J. A., Whittet D. C. B., Evans A., Albinson J. S., 1987, Nature, 329, 519
Brasseur C. E., Phillip C., Fleming S. W., Mullally S. E., White R. L., 2019, Astrocut: Tools for creating cutouts of TESS images (ascl:1905.007)
Brewer J. M., Fischer D. A., Valenti J. A., Piskunov N., 2016, ApJS, 225, 32
Brunschweiger J., Greiner J., Ajello M., Osborne J., 2009, A&A, 496, 121
Chambers K. C., et al., 2016, arXiv e-prints, p. arXiv:1612.05560

Chanmugam G., Wagner R. L., 1977, ApJ, 213, L13
Claret A., 2000a, A&A, 359, 289
Claret A., 2000b, A&A, 363, 1081
Claret A., Diaz-Cordoves J., Gimenez A., 1995, A&AS, 114, 247
Cox A. N., 2000, Allen's astrophysical quantities. Springer-Verlag, New York
Crampton D., Cowley A. P., Fisher W. A., 1986, ApJ, 300, 788
Cropper M., 1990, Space Sci. Rev., 54, 195
Cropper M., Wu K., Ramsay G., Kocabiyik A., 1999, MNRAS, 306, 684
Dougherty S. M., Waters L. B. F. M., Bode M. F., Lloyd H. M., Kester D. J. M., Bontekoe T. R., 1996, A&A, 306, 547
Eggleton P. P., 1983, ApJ, 268, 368
Evans P. A., Hellier C., 2007, ApJ, 663, 1277
Ezuka H., Ishida M., 1999, ApJS, 120, 277
Faulkner J., Flannery B. P., Warner B., 1972, ApJ, 175, L79
Foreman-Mackey D., Hogg D. W., Lang D., Goodman J., 2013, PASP, 125, 306
Gaia Collaboration et al., 2018, Astronomy & Astrophysics, 616, A1
Gallagher J. S., Oinas V., 1974, PASP, 86, 952
Garlick M. A., Mittaz J. P. D., Rosen S. R., Mason K. O., 1994, MNRAS, 269, 517
Gazeas K., 2016, in Revista Mexicana de Astronomia y Astrofisica Conference Series. pp 22–23
Gray D. F., 1992, The Observation and Analysis of Stellar Photospheres. Cambridge University Press, Cambridge
Hachisu I., Kato M., 2006, ApJS, 167, 59
Hachisu I., Kato M., 2007, ApJ, 662, 552
Hachisu I., Kato M., 2015, ApJ, 798, 76
Harrison T. E., 2016, ApJ, 833, 14
Harrison T. E., Hamilton R. T., 2015, AJ, 150, 142
Harrison T. E., Bornak J., McArthur B. E., Benedict G. F., 2013, ApJ, 767, 7
Henden A. A., Honeycutt R. K., 1995, PASP, 107, 324
Henden A. A., Honeycutt R. K., 1997, PASP, 109, 441
Hudec R., 1981, Bulletin of the Astronomical Institutes of Czechoslovakia, 32, 93
Jönsson H., et al., 2020, AJ, 160, 120
Kepler S. O., et al., 2016, MNRAS, 455, 3413
Kim S.-W., Wheeler J. C., Mineshige S., 1992, ApJ, 384, 269
King A. R., 1988, QJRAS, 29, 1
Koen C., Kilkenny D., van Wyk F., Marang F., 2010, MNRAS, 403, 1949
Kraft R. P., 1964, ApJ, 139, 457
Kurucz R. L., 1996, in Adelman S. J., Kupka F., Weiss W. W., eds, Astronomical Society of the Pacific Conference Series Vol. 108, M.A.S.S., Model Atmospheres and Spectrum Synthesis. p. 2
Landi R., Bassani L., Dean A. J., Bird A. J., Fiocchi M., Bazzano A., Nousek J. A., Osborne J. P., 2009, MNRAS, 392, 630
Lightkurve Collaboration et al., 2018, Lightkurve: Kepler and TESS time series analysis in Python (ascl:1812.013)
Liimets T., Corradi R. L. M., Santander-García M., Villaver E., Rodríguez-Gil P., Verro K., Kolka I., 2012, ApJ, 761, 34
Luck R. E., 2015, AJ, 150, 88
Marsh T. R., 1989, PASP, 101, 1032
Marsh T. R., Robinson E. L., Wood J. H., 1994, MNRAS, 266, 137
Morales-Rueda L., Still M. D., Roche P., Wood J. H., Lockley J. J., 2002, MNRAS, 329, 597 (MR02)
Nauenberg M., 1972, ApJ, 175, 417
Norton A. J., Wynn G. A., Somerscales R. V., 2004, ApJ, 614, 349
Patterson J., 1991, PASP, 103, 1149
Patterson J., 1994, PASP, 106, 209
Pecaut M. J., Mamajek E. E., 2013, ApJS, 208, 9
Pottasch S., 1959, Annales d'Astrophysique, 22, 412
Reinsch K., 1994, A&A, 281, 108
Revnivtsev M., Churazov E., Postnov K., Tsygankov S., 2009, A&A, 507, 1211
Revnivtsev M., Potter S., Kniazev A., Burenin R., Buckley D. A. H., Churazov E., 2011, MNRAS, 411, 1317
Ricker G. R., et al., 2015, Journal of Astronomical Telescopes, Instruments, and Systems, 1, 014003
Sabbadin F., Bianchini A., 1983, A&AS, 54, 393

Scott A. D., Rawlings J. M. C., Evans A., 1994, MNRAS, 269, 707
Seaquist E. R., Bode M. F., Frail D. A., Roberts J. A., Evans A., Albinson J. S., 1989, ApJ, 344, 805
Shahbaz T., Watson C. A., Dhillon V. S., 2014, MNRAS, 440, 504
Shara M. M., Prialnik D., Hillman Y., Kovetz A., 2018, ApJ, 860, 110
Steeghs D., Jonker P. G., 2007, ApJ, 669, L85
Stockman H. S., Schmidt G. D., Berriman G., Liebert J., Moore R. L., Wickramasinghe D. T., 1992, ApJ, 401, 628
Suleimanov V., Revnivtsev M., Ritter H., 2005, A&A, 435, 191
Suleimanov V., Doroshenko V., Ducci L., Zhukov G. V., Werner K., 2016, A&A, 591, A35
Suleimanov V. F., Doroshenko V., Werner K., 2019, MNRAS, 482, 3622
Torres M. A. P., Casares J., Jiménez-Ibarra F., Álvarez-Hernández A., Muñoz-Darias T., Armas Padilla M., Jonker P. G., Heida M., 2020, ApJ, 893, L37
Wada Y., Yuasa T., Nakazawa K., Makishima K., Hayashi T., Ishida M., 2018, MNRAS, 474, 1564
Warner B., 1995, Cambridge Astrophysics Series, 28
Watson M. G., King A. R., Osborne J., 1985, MNRAS, 212, 917
Webbink R. F., Rappaport S., Savonije G. J., 1983, ApJ, 270, 678
Webbink R. F., Livio M., Truran J. W., Orio M., 1987, ApJ, 314, 653
Williams A. S., 1901, MNRAS, 61, 337
Yaron O., Prialnik D., Shara M. M., Kovetz A., 2005, ApJ, 623, 398
Yee S. W., Petigura E. A., von Braun K., 2017, ApJ, 836, 77
Ziółkowski J., Zdziarski A. A., 2020, MNRAS, 499, 4832
Zorotovic M., Schreiber M. R., Gänsicke B. T., 2011, A&A, 536, A42
Šimon V., 2002, A&A, 382, 910

This paper has been typeset from a TEX/LATEX file prepared by the author.